Electrochimica Acta 534 (2025) 146552

Contents lists available at ScienceDirect

Electrochimica Acta

journal homepage: www.journals.elsevier.com/electrochimica-acta

N-doped hard carbon with closed-pore structure via a high-pressure nitrogen doping approach as anodes for Sodium-ion batteries

Zhi-Ting Liu[a], Tzu-Hsien Hsieh[b], Cheng-Wei Huang[b], Choah Kwon[c], Ju Li[c], Jun-Yang You[d], Chin-Jung Lin[e], Wei-Ren Liu[a,f,g,*]

[a] *Department of Chemical Engineering, R&D Center for Membrane Technology, Chung Yuan Christian University, 200 Chung Pei Road, Chungli District, Taoyuan City, 32023, Taiwan*
[b] *Green Technology Research Institute, CPC Corporation, Taiwan, No. 2, Zuonan Road, Nan-Tsu District, Kaohsiung, 81126, Taiwan*
[c] *Department of Nuclear Science and Engineering and Department of Materials Science and Engineering, Massachusetts Institute of Technology, Cambridge, MA 02139, USA*
[d] *Department of Environmental Engineering, National Ilan University, No. 1, Section 1, Shennong Road, Yilan City, Yilan, 260007, Taiwan*
[e] *Graduate Institute of Environmental Engineering, National Central University, 300 Zhongda Rd., Zhongli Dist., Taoyuan City 32001, Taiwan*
[f] *Hierarchical Green-Energy Materials (Hi-GEM) Research Center, National Cheng Kung University, 1 University Road, Tainan 70101, Taiwan*
[g] *Department of Chemical Engineering, Faculty of Engineering, Chulalongkorn University, Bangkok 10330, Thailand*

ARTICLE INFO

Keywords:
Biomass carbon
Sodium ion batteries
Anode
Nitrogen doping
DFT calculations
Pouch cells

ABSTRACT

The slow diffusion kinetics of Na^+ at low potential constitute a significant hurdle to high-power applications, even though the intercalation mechanism of hard carbon (HC) anodes for sodium-ion batteries (SIBs) achieves respectable electrochemical performances. This study investigates nitrogen (N) doping effects on the electrochemical performance of HC for SIBs' applications. X-ray photoelectron spectroscopy (XPS) analysis indicates that the N content of the high-temperature sintering process (HT-NHC) and high-pressure hydrothermal process (HP-NHC) impacts the N incorporation into the HC structure. The content of pyridinic N in HP-NHC is 9.9 mol %, which is higher than that in HT-NHC of 6.0 mol %. After 200 cycles, HP-NHC delivered a high reversible capacity of 331 mAh/g at 0.5 A/g. The improved electrochemical performance of HP-NHC is attributed to the multiplier effects of N-doping, which improves the Na^+transfer rate. The results of theoretical calculations indicate a weak electrostatic interaction between Na^+ and graphite and graphitic nitrogen functional groups on the surfaces in HC materials (HCMs). Moreover, the defects, pyrrolic N, N-oxides, and pyridinic N benefit Na^+ adsorption. Pyrrolic N and other N-containing functional groups offer adequate adsorption sites for Na^+ and hence boost the capacity of HT-NHC and HP-NHC, supporting the results of our investigation.

1. Introduction

Lithium-ion batteries (LIBs) are extensively applied in portable electronic devices and electric vehicles [1–3]. With the ever-increasing demands on different energy storage devices for various applications, sodium-ion batteries (SIBs) operating with similar reaction mechanisms as those of LIBs enter the energy storage field as an alternative [4,5]. Although SIBs generally have a lower specific energy density than LIBs, SIBs have many advantages over LIBs, such as absence of expensive materials such as Co, Ni, Cu, Li and graphite, higher storage safety from being able to discharge to zero voltage and a wider operation temperature [6–16]. SIBs have higher rate performance than LIBs due to lower solvation energy, stronger interfacial ion diffusion ability, and higher ionic conductivity of the Na^+ conductive liquid electrolyte [17]. Among these advantages, hard carbon (HC) as the anode material for SIBs provides better environmental benignity, higher sustainability, lower price, and higher specific capacity than those of the graphite anode in LIBs because HC can be made from low-cost biowaste materials with a much lower processing temperature [18–20].

Biomass carbons (BCs) can be made from green tea wastes [21], bacterial celluloses [22], coir pith [23], orange peels [24], garlic peels [25] and so on [26–31]. To improve the electronic conductivity of HCs, doping technique is typically effective for altering the inherent characteristics of materials, modifying surface chemistry, and producing local alterations to the elemental makeup of host materials [32–35]. These foreign doping atoms, such as sulfur (S) [36–38], phosphorus (P) [39,

---

* Corresponding author.
E-mail address: wrliu@cycu.edu.tw (W.-R. Liu).

https://doi.org/10.1016/j.electacta.2025.146552
Received 14 February 2025; Received in revised form 4 May 2025; Accepted 25 May 2025

40] and nitrogen (N) [41–43], have been widely used as potential candidates to enhance the electrochemical performance of carbon-based anode materials for LIBs' and SIBs' applications [44]. However, due to their larger atomic radii and lower electronegativities, S and P dopants cause structural deformation that alters the charge density of HCs.

The synthesis of carbonaceous materials is often accomplished via hydrothermal carbonization (HTC). HTC was discovered in 1911 by Friedrich Bergius [45]. In his study, peat was used as the carbon source for the HTC process, which led to the production of a significant amount of CO. Coal formation is mimicked by the carbonaceous residue produced by this process. To produce carbon microspheres from monosaccharides, the HTC method was rediscovered in 2015 [46]. Zhao et al. proposed an HTC treatment of glucosamine hydrochloride and chitosan generated from biomass at a lower temperature of 180 °C [47]. The resulting N-doped carbon showed little porosity, a low specific surface area of <10 m^2 g^{-1} and an amorphous structure under 180 °C hydrothermal condition. In addition, with the reaction temperature increased, the structure of N-doped carbon slightly became crystalline due to the assembling of turbostatic carbon. Fedoseeva *et al.* proposed a pore size-tunable N-doped carbon material with some defects and functional groups by changing the synthesis temperature and etching condition via a hydrothermal treatment in the ammonia solution at 147 °C for 30 h [48]. The unique hydrothermal etching process not only resulted in the micropores and tiny mesopores but also enhanced the extra specific surface area and pore volume. The ammonia-created pore structure in carbon provided higher reversible capacity and rate capability due to these activation-induced micropores and functional groups, including nitrogen and oxygen. The Na^+ storage capacity by 100 mAh g^{-1} in SIB was achieved by the synergistic effects of large micropores with a size of 1.4 nm and an enhanced content of N and carbonyl functional group edge in the ammonia-assisted treated N-doped carbon. The design of porous N-doped carbon compounds would greatly benefit electrochemical applications from these findings.

Nie et al. proposed an *in-situ* polymerization process by employing palm leaf as the carbon precursor and polyaniline as the nitrogen source to yield a mesoporous N-doped palm leaf-based hard carbon (PLHC—N), which could buffer the volume expansion during charge and discharge processes, increase ion transport channels and enhance exceptional Na^+ storage capacity [49]. The *in-situ* N-doping process successfully generated these additional active sites for Na storage and both ionic and electronic conductivities were enhanced in transferability. The PLHC—N sample exhibited an impressive adsorption-intercalation-hole filling storage mechanism, enabling it to achieve long-term cycle stability at 200 mA g^{-1} and the retention was close to 95 % after 1000 cycles and an ultrahigh reversible capacity of 373 mAh g^{-1} at 25 mA g^{-1}.

In this study, we focused on experimental and theoretical calculations to investigate the sodiation/desodiation mechanism. We fabricate a pouch-type full cell to demonstrate a practical application using HP-NHC as an anode and $Na_3V_2(PO_4)_3$ as a cathode. The outstanding electrochemical performance revealed that the hydrothermal N doping process is a potential approach for applications in SIBs.

2. Experimental section

2.1. Material preparations

The waste sawdust (HC-Bare) was provided by Green Technology Research Institute, Chinese Petroleum Corporation®, Taiwan. The HCl pre-treatment washing process was carried out to eliminate possible metal impurities in HC-Bare [50]. The experiments of these two different N-doped HC samples were described below: (i) High-temperature sintering process: 1.0 g of HCl-treated HC-Bare was mixed with 10 g urea in an alumina crucible and raised to 900 °C under Argon gas for 3 h to form desired N-doped HC, namely HT-NHC; (ii) High-pressure hydrothermal process: 0.25 g HCl-treated HC-Bare and 2.5 g urea were dissolved in 30 mL distilled water to poured into the Teflon container within an autoclave to react at 160 °C for 24 hr. Then, the solution was washed until pH≈7 by distilled water. Finally, the powder was dried at 80 °C overnight. HP-NHC noted the obtained sample.

2.2. Characterizations

Raman spectra (Witec alpha300R) and X-ray diffraction (XRD, Bruker D2) were used to identify the crystal structure and defects of HCMs. Raman micro-spectroscopy was carried out using a solid-state laser with a 532 nm wavelength, a power of 1.6 mW and a 600 lines/mm grating. The Raman spectra were collected with a point focus lens and a 50x objective on an area of 60 μm × 60 μm with 60 points per line and 60 lines per image. Each spectrum at each point was collected with 1.5 s integration time. The collected spectra were corrected for cosmic rays and averaged to obtain a representative spectrum for each sample. X-ray photoelectron spectroscopy (XPS, JEOL Photoelectron Spectrometer (ESCA), JPS-9200 and monochromatic (Al-K) were used to determine the surface chemistries of HC-Bare, HT-NHC and HP-NHC. The N_2 adsorption/desorption isotherms were measured by using a Tristar 3000. CO_2 uptake by the fabricated samples was determined using weight variations in pure CO_2 flow at ambient pressure, as measured by thermogravimetric analysis (TA Instruments SDT-Q600). Before CO_2 uptake, all samples were preheated at 120 °C for 1 h under pure nitrogen flow (50 mL/min) in the TGA sample chamber. Approximately 5 mg of the sample was placed and heated to 30 °C under N_2 atmosphere (50 mL/min), then the flow gas was immediately switched to pure CO_2 (50 mL/min). At the same time, the sample was heated to 120 °C at a rate of 5 °C/min. Scanning electron microscopy (SEM, JSM-7600F, JEOL Ltd.) and high-resolution transmission electron microscopes (HR-TEM, JEM2100, JEOL Ltd.) were used to examine the microstructure morphology of HC-Bare, HT-NHC and HP-NHC.

2.3. Electrodes preparation

To make the anode electrode, 70 wt. % active material, 20 wt. % Super P (Timcal®), 6 wt. % carboxymethyl cellulose and 4 wt. % styrene-butadiene rubber binde were used for slurry preparation. Deionized water was used as the solvent for the slurry. The slurry was then evenly tape-casted on a piece of Cu-foil. The coated Cu-foil was dried under vacuum at 120 °C for 10 hr. The electrodes were subsequently punched out of the Cu foil into round-shaped disks with a 1.4 cm diameter. The mass loading of the HC-based electrode is 1.6–1.9 mg cm^{-2} with ~ 40 μm in thickness.

The $Na_3V_2(PO_4)_3$ (NVP) cathode (NVP-20 μm) was provided by Shenzhen KeJing Star Technology Company. The slurry for positive electrode was made by 90 wt. % of NVP as the active material, 5 wt. % of Super P (Timcal®) as the electronic conductive additive, 5 wt. % of polyvinylidene difluoride (Kynar®, 99.99 %) as the binder to mix in N-Methyl-2-pyrrolidone (Alfa Acer, 99.99 %). The slurry was then evenly tape-casted on a piece of Al-foil. The coated Al-foil was dried under a vacuum at 120 °C for 10 h. The mass loading of NVP in the electrode material is 4.5 mg cm^{-2}.

2.4. Electrochemical measurements

CR2032 coin cells were used for the electrochemical tests with the fabricated electrodes and glass fiber (Pall Corporation) as the separator. The liquid electrolyte is 1 M $NaClO_4$ (Alfa Acer, 99.99 %) dissolved in propylene carbonate (PC, Sigma-Aldrich, 99.9 %) and 5 % fluoroethylene carbonate (FEC, Sigma-Aldrich, 99.9 %). The coin cell assembly was carried out in a glove box under an Argon atmosphere, with oxygen and moisture levels below 0.5 ppm. The discharge-charge processes were implemented at various current densities in the voltage window between 0.01–3.0 V (V vs. Na/Na^+) using the AcuTech battery testing system (Taiwan, R.O.C, model 750B). The cyclic voltammetry (CV) was carried out with scan rates of 0.1–0.5 mV/s in a voltage window of 0.01–3 V (V vs. Na/Na^+). Electrochemical impedance measurements were conducted by using a potentiostat (SP-50e) in the frequency range 10 mHz-1 MHz with a perturbation AC voltage of 5 mV. For pouch cell assemblings, we used NVP as the cathode, HP-NHC as the anode and polypropylene as the separator (Foresight Energy Tech., Taiwan) to fabricate a single layer of soft-packed pouch cell. A separator was layered between one cathode and one anode sheet measuring 33 mm by 34 mm. With a dew point temperature of −45 °C, the pouch-type SIB cells were sealed in a dry room. Then, the cells were drenched in electrolyte for 6 h before the electrochemical tests were carried out.

2.5. Theoretical calculations

Spin-polarized density functional theory (DFT) was employed to understand the diffusion mechanisms of Na^+ in the N-doped HC, which is implemented in Vienna ab initio simulation package (VASP) with projector augmented wave (PAW) method of pseudopotential and Perdew-Burke-Ernzerhof (PBE) of generalized gradient approximation (GGA) as exchange-correlation functional, respectively [51–54]. The Vander Walls corrections of the D3 method were included in the calculations [55,56] We set up the convergence criteria of the energy and force as 10^{-5} eV and 0.02 eV/Å and Monkhorst-Pack grids of 7 × 7 × 1, respectively. The diffusion activation energies of the Na^+on the model systems were obtained by climbing nudged elastic band (CI-NEB) method under criteria of 0.02 eV/Å.

3. Results and discussion

Scheme 1

The SEM images of HC-Bare, HT-NHC and HP-NHC are shown in Fig. 1 (a-c), respectively. These samples showed a sheet-stacking-like structure. Fig. 1 (d-e) show the elemental distribution of HP-NHC from the EDX mappings. The corresponding elemental mappings yielded ~93.2, ~5.5 and ~1.3 wt. % for C, O and N, respectively. The SEM images and EDX mappings of pristine HC-Bare and HT-NHC are also shown in Fig. S1 and Fig. S2 to compare the difference in surface morphology with or without N doping. As shown in Fig. S1, two signals of C and O in HC-Bare were detected with ~92.8 and ~7.2 wt. %, respectively. The C, O, and N elements were homogeneously distributed in HT-NHC with ~91.1, ~8.2 and ~0.7 wt. %, respectively. HRTEM has been widely used to study the microstructure of hard carbon and has confirmed the presence of closed pores [73–77]. These closed pores are primarily formed by disordered carbon layers and play a crucial role in the sodium-ion storage mechanism of hard carbon. Research shows that highly crystalline cellulose decomposes during carbonization into long-range carbon layers, forming the walls of closed pores, while the amorphous components hinder graphite-like crystallization, inducing curvature in the carbon layers. Our analysis has also verified the existence of closed pores using this approach, further reinforcing their structural significance and impact on material performance, as shown in Fig. S3. Fig. S3(a-c) show HRTEM images of HCMs. The crystalline domains of HCMs was not obvious, similar to traditional amorphous carbon-based material. Generally, these amorphous hard carbons had a larger interlayer spacing and smaller crystalline domains compared to crystalline graphite, which allowed hard carbon-based anodes to store more charges in the same volume and exhibited faster kinetics, which further improved larger reversible capacity, rate capability as well as cycle stability, especially for SIBs' applications due to much-alleviated volume expansion and contraction of HC-based anodes during the charge (sodiation) and discharge (dissociation) processes.

The XRD patterns of HCMs are displayed in Fig. 1(g-i). We used 10 wt. % Al_2O_3 as the internal standard material for 2-theta calibration. Two broad peaks at 23° and 43° corresponded to the (002) and (100) planes of HCMs, respectively. The lattice parameters c values of HC-Bare, HT-NHC and HP-NHC were refined to be ~7.39, ~7.41 and ~7.43 Å, respectively. Slightly cell volume expansions of HCs were observed after these two N doping processes. To study how N-doped affected d-spacing in the (002) plane, we used Braad's law to calculate d-spacings of HC-Bare, HT-NHC and HP-NHC and the corresponding results were shown in Fig. S4(a-c). In addition, the detailed graphite microcrystalline parameters (L_c, L_a d_{002}, N) analyzed by XRD and HRTEM is summaried in Table S1. We calculated the values using Eq (1):

$$L(nm) = \frac{K\lambda}{\beta cos\theta} \tag{1}$$

where K values are 1.84 for the (100) peak and 0.90 for the (002) peak, λ is the X-ray wavelength (1.5418 Å), β is the full width at half maximum (FWHM) of the corresponding diffraction peaks, and θ is half of the diffraction angle (2θ). The number of stacked graphene layers (N) was determined by Lc/d_{002}.

Sun et al. indicated that a pseudo-graphitic structure with a d-spacing of 0.36–0.4 nm is suitable for intercalating and extracting Na^+ [57]. In contrast, a graphite-like structure with a smaller d-interlayer spacing of <0.36 nm cannot accommodate Na^+ [57,58]. The N_2 adsorption/desorption isotherms of HCMs and the corresponding data are depicted in Fig. 1(k) and Table 1, respectibely. From Fig. 1(k), HCMs all exhibited type I hysteresis loops. In type I hysteresis loops, the adsorption amount increases rapidly at low relative pressure and the adsorption reaches a saturation value after reaching a certain relative pressure. Generally, type I isotherms tend to be filled with micropores. The specific surface

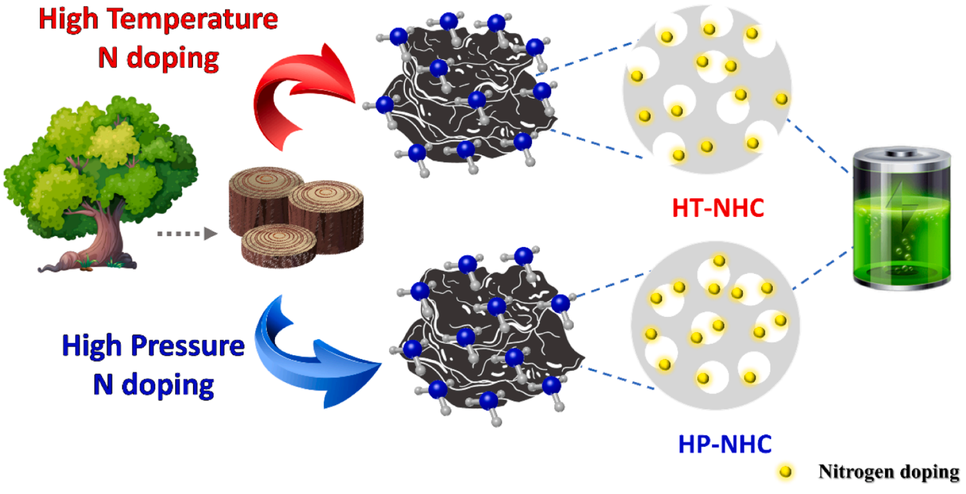

Scheme 1. Schematic illustrations of the preparation of HCMs.

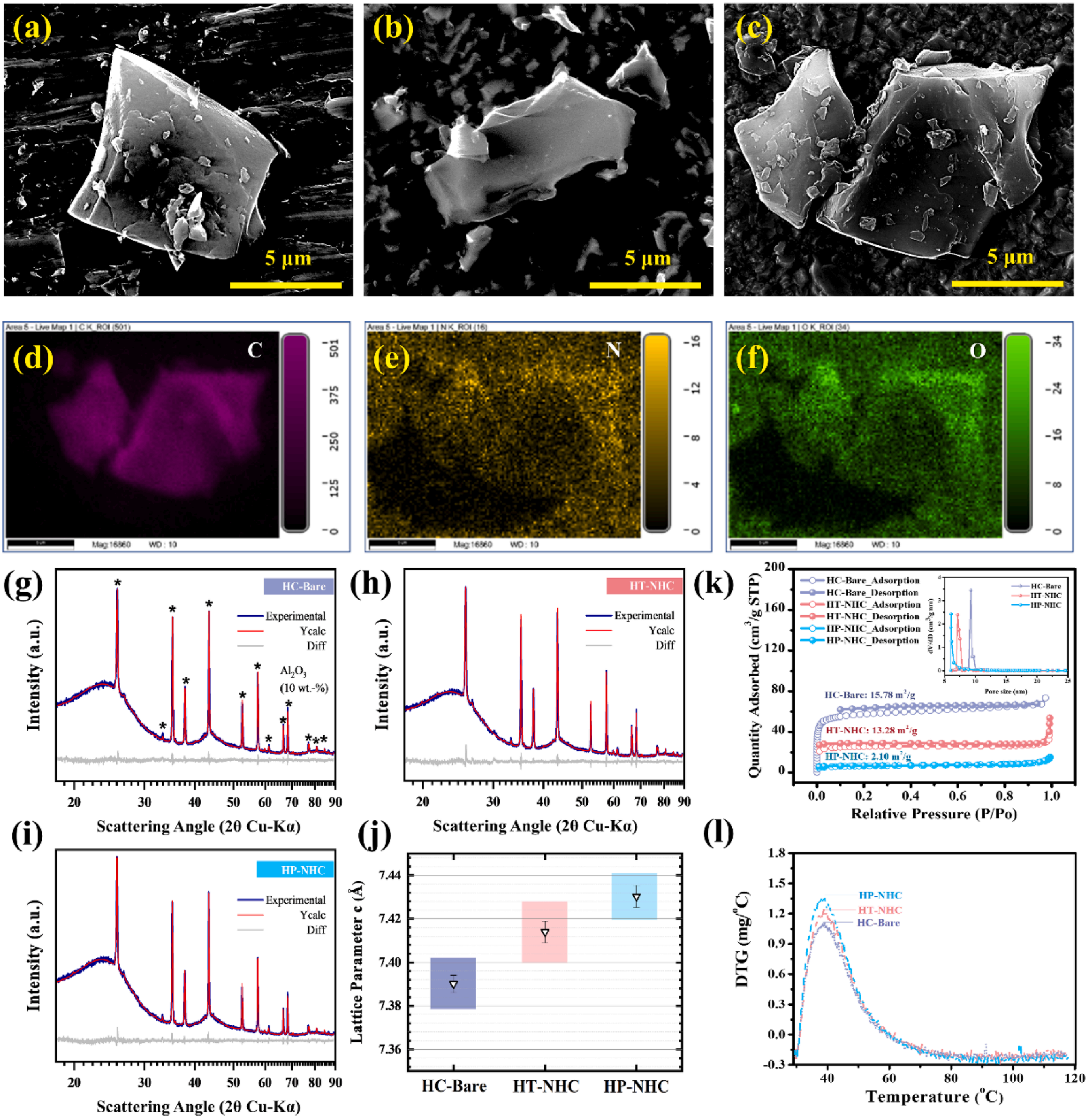

Fig. 1. SEM images of (a) HC-Bare, (b) HT-NHC and (c) HP-NHC; (d-f) EDX analysis of HP-NHC; XRD patterns of (g) HC-Bare, (h) HT-NHC and (i) HP-NHC; (j) The lattice parameter *c* of HCMs; (k) N_2 adsorption/desorption isotherms (Inset: The corresponding pore size distributions); CO_2 uptake by the obtained samples in pure CO_2 atmosphere; (l) Derivative thermogravimetry curves of the sorbents corresponding to Fig. S5(a).

Table 1
The specific surface area, pore volume, and pore size of HCMs.

Samples	SSA (m^2/g)	Pore Volume (cm^3/g)	Pore Size (nm)	Meso-pore (%)	Micro-pore (%)
HC-Bare	15.8	0.0205	5.19	26.9	73.1
HT-NHC	13.3	0.0234	7.01	18.1	81.9
HP-NHC	2.1	0.0132	3.27	6.4	93.6

area (SSA) of HC-Bare, HT-NHC and HP-NHC were 15.8, 13.3 and 2.1 m^2/g, respectively. It is worth mentioning that HP-NHC has the lowest SSA compared to HC-Bare and HT-NHC. To explain further why the SSA of HP-NHC was smaller than that of HT-NHC, As shown in Table 1, the pore volume of HC-Bare, HT-NHC and HP-NHC was 0.021, 0.023 and 0.013 cm^3/g, respectively. The percentages of mesopore and micropore were 26.9 and 73.1 % in HC-Bare, while that for HP-NHC were 6.4 and 93.6 %, respectively [59]. It is known that the Na^+ mechanism and the microporous structures can facilitate Na^+ diffusion by providing more pathways, thereby increasing the diffusion rate and enhancing the storage capacity [50,57]. Additionally, the microporous structure can enhance HCMs’ cycle stability, allowing for stable long-term storage of Na^+ and improving the storage capacity as a result [50,57,60]. Tai et al. provided feasible solutions by introducing phenolic-formaldehyde resin-derived HCs with tunable microporous structures [61]. According to Tai’s study, different gases, like N_2, O_2 and CO_2 can verify the micropore structure. Follow this idea: if N_2 only adsorbed open pores instead of closed pores, we speculated more closed pores in HP-NHC because of its lower SSA. Thus, to further confirm the exist of closed pores in HCMs, we replaced N_2 with CO_2 to carry out adsorption tests at two different conditions, isotherm CO_2 absorption and temperature-dependence CO_2 adsorption tests in Fig. 1(l) and Fig. S5(a-b). From Fig. S5(a), the CO_2 uptake after 120 min for HC-Bare, HT-NHC and HP-NHC were 70.7, 75.0 and 81.2 mg CO_2 / g-sorbents. Active closed pores are closed micropores that serve the same purpose as the interlayer spacing in HC. Fig. S5(b) summarizes the CO_2 uptake performance of the obtained samples in a pure CO_2 atmosphere over a temperature range from 30 °C to 120 °C. The HC-Bare sample presented low CO_2 sorption performance (maximal uptake of 15.7 mg/g). HT-NHC and HP-NHC reached a maximal weight increase of 17.2 mg/g and 19.2 mg/g at 60 °C, respectively. However, beyond 60 °C, the sorbent released CO_2 (weight decrease). Furthermore, compared with HC-Bare, the CO_2 uptake was markedly improved for HP-NHC and HT-NHC. In particular, the CO_2 uptake process presented specific variations, as shown in Fig. 1(l) (DTG, derivative thermogravimetry curve). There was only one strong peak at ~40 °C for these three samples, where the maximal CO_2 sorption rate occurs. Compared with HC-Bare, the reaction rates and the maximal sorption capacities of HP-NHC and HT-NHC were significantly enhanced. At a high-temperature N doping process, NH_3 was formed from the decomposition of urea. High temperatures cause HCMs to collapse to provide lower SSA [50,61]. On the contrary, for HP-NHC, the high-pressure condition created more closed pores inside the structure of HC.

As depicted in Fig. 2(a-c) and Table 3, we can accurately evaluate the content of C/N and the chemical bondings of HCMs from XPS analyses. The survey XPS spectra of HCMs are displayed in Fig. 2(a). The peaks of C1s and O1s of HC-Bare were located at 283.8 and 533.7 eV, respectively. By integrating these two peak areas, the molar concentrations of C and O in HC-Bare were determined to be 85.6 % and 14.4 %, as shown in Table 2. Fig. 2(b) shows the high-resolution XPS spectra of HCMs for C1s. Three peaks were located at 284.2, 285.9 and 288.3 eV, corresponding to $C=C$/C—C, C—N/C—O and $C=O$/O—$C=O$. For the N1s spectra (Fig. 2(c)), the measured peak can be deconvoluted into four peaks at 397.8, 398.6, 399.9, and 401.6 eV, which can be attributed to pyridinic N (N6), pyrrolic N (N5), graphitic N (GN), and N-oxide (NO), respectively. As shown in Table 3, N6 was 6.0 mol. % in HT-NHC and 9.9 mol. % in HP-NHC, while N5 was 23.3 % in HT-NHC and 25.7 % in HP-NHC. Moreover, the percentage of GN was 49.9 % in HT-NHC and 45.0 % in HP-NHC, and NO was 20.8 % in HT-NHC and 19.4 % in HP-NHC. HP-NHC with higher N6 percentage and more active sites for Na^+ storage, which can facilitate the sodiation and desodiation during charge and discharge processes [62–65].

Table 2
The contents of C, O and N (atomic %) were determined from XPS spectra.

Samples	C (%)	O (%)	N (%)
HC-Bare	85.64	14.36	–
HT-NHC	88.02	7.46	4.52
HP-NHC	89.15	7.74	3.11

Fig. 3(a-c) show Raman spectra of HC Bare, HT-NHC and HP-NHC, respectively. The G-band from the carbon plane stretching motion between sp [2] carbon atoms and the D-band from a disordered band originating in structural can be deconvoluted into subpeaks D1, D3, D4 and G, where D1 peak (1326 cm^{-1}) can be attributed to disordered carbon or graphite flaws near the graphite’s edge, D3 peak (1501 cm^{-1}) is the short-range sp [3] carbon vibration of HCMs and D4 peak (1182 cm^{-1}) indicates the disordered graphite lattice and G peak (1598 cm^{-1}) refers to the ordered graphite structure [24]. The D3/G ratio of HP-NHC

Table 3
The ratio of pyridinic N, pyrrolic N, graphitic N and N-oxide were determined from the XPS spectra of N 1 s according to the fitting curves.

Samples	Pyridinic N (%)	Pyrrolic N (%)	Graphitic N (%)	N-oxide(%)
HT—NHC	6.0	23.3	49.9	20.8
HP-NHC	9.9	25.7	45.0	19.4

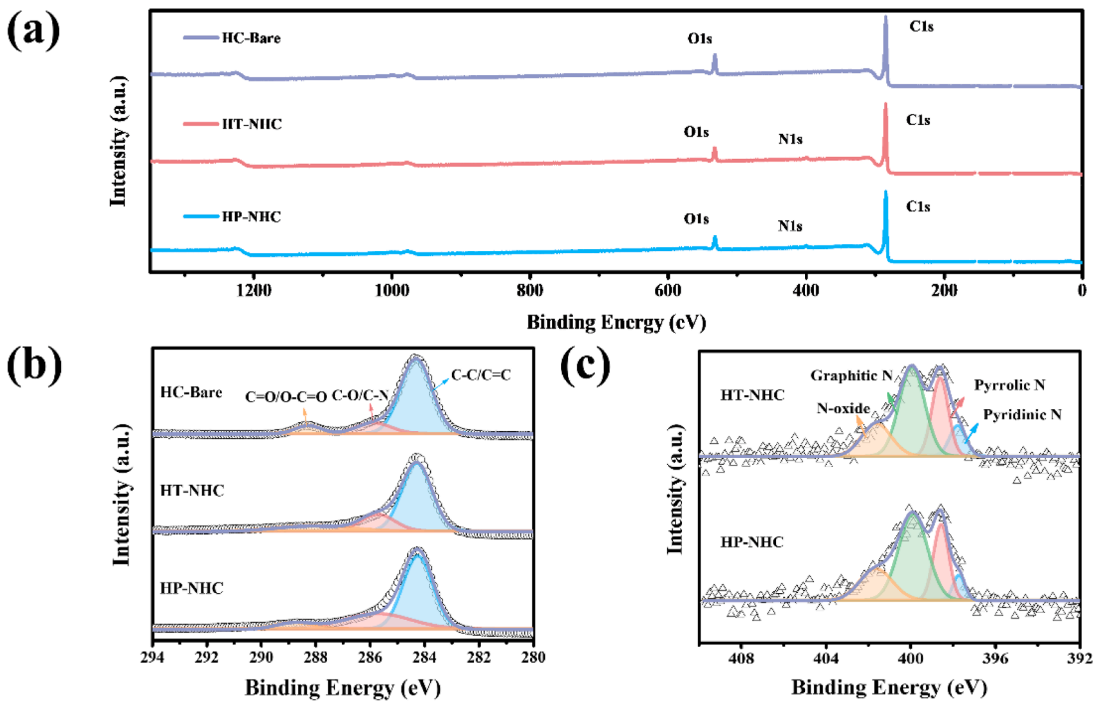

Fig. 2. (a) XPS spectra of HCMs and (b) High-resolution XPS spectra of C1s; (c) High-resolution XPS spectra of N1s of HCMs.

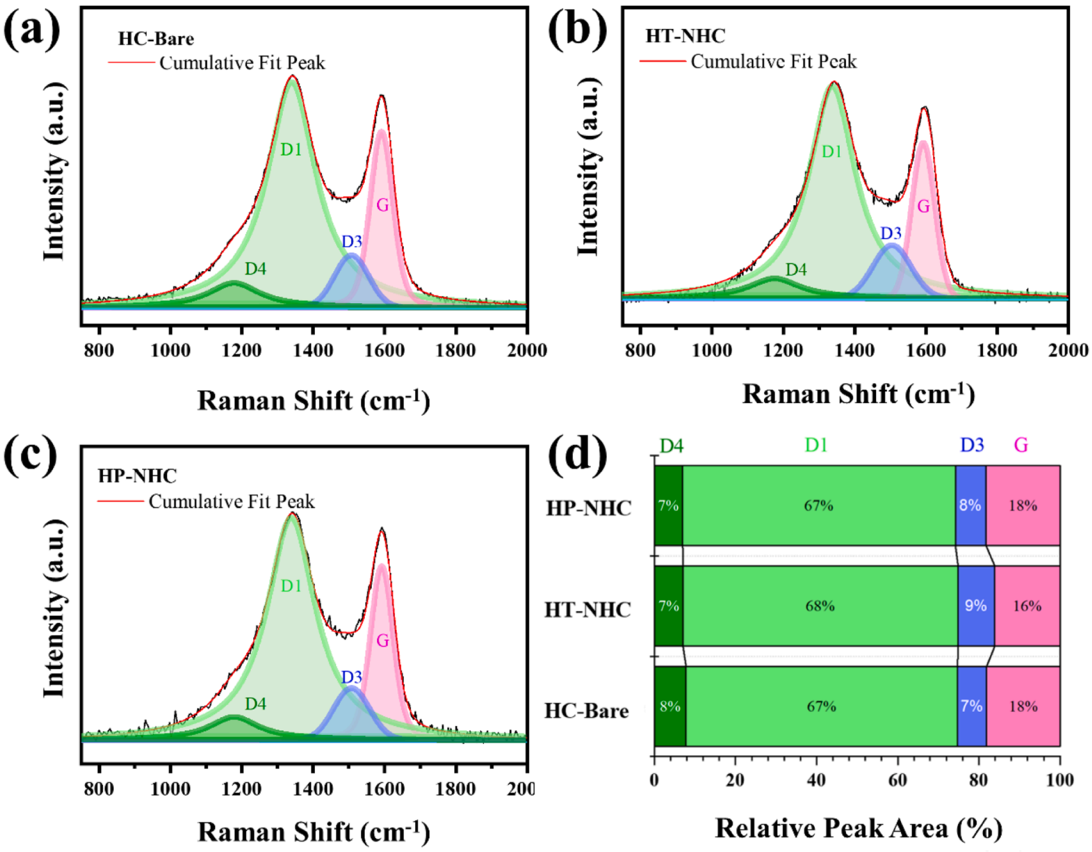

Fig. 3. Gauss decomposition of the Raman spectrum for (a) HC-Bare, (b) HT-NHC and (c) HP-NHC; (d) The Gauss decomposition ratio of HCMs.

and HT-NHC was higher than that of HC-Bare, indicating that there were more active sites and structural defects in HP-NHC and HT-NHC for Na^+ storages, as shown in Fig. 3(d) [62–65].

Fig. 4(a-b) show charge and discharge curves of HC-Bare and HP-NHC at 0.1 A/g for first three cycles, respectively. At the first cycle, HC-Bare exhibited a reversible capacity of 152 mAh g^{-1} with a coulombic efficiency (CE) of 53.9 %. HP-NHC showed a reversible capacity of 357 mAh g^{-1} with a CE of 63.7 %. Fig. 3(c-d) show the charge/discharge curves of HC-Bare and HP-NHC at the 5th, 10th, 50th, 100th and 200th cycles. The average reversible capacities in HC-Bare and HP-NHC were 137 and 348 mAh g^{-1} at 0.1 A g^{-1} after the first three cycles, respectively. The reversible capacities of HC-Bare and HP-NHC were found to be 116 and 298 mAh g^{-1} after 200 cycles at the same current density. In addition, the capacity retentions of HC-Bare and HP-NHC were 84.5 % and 85.7 % after 200 cycles, respectively, representing the cyclic stability of HP-NHC, which was higher than that of HC-Bare. Fig. 4(e) displays the rate performances of HCMs at various current densities. The average reversible capacities of HC-Bare at 0.1, 0.2, 0.5, 1.0, 2.0 and 5.0 A/g were 201, 197, 151, 119, 93 and 66 mAh/g, respectively. The average reversible capacities of HT-NHC at 0.1, 0.2, 0.5, 1.0, 2.0 and 5.0 A/g were 330, 317, 284, 261, 212 and 149 mAh/g, respectively. The average reversible capacities of HP-NHC at 0.1, 0.2, 0.5, 1.0, 2.0 and 5.0 A/g were 351, 320, 300, 275, 247 and 193 mAh/g, respectively. By facilitating charge transfer and enhancing electrochemical activity, N6 can improve the performance of electrodes in energy storage devices such as SIBs [41]. The slope region above 0.01 V vs. Na/Na^+ is suggested to be the Na^+ storage occurring at defect sites on the surface of active materials [24,28]. Lower graphitic order and oxygen functional groups led to the plateau region below 0.01 V vs. Na/Na^+ [24,28]. It is a challenge for Na^+ to intercalate into the graphitic layer structure during the sodiation process. This phenomenon indicated that the Na^+ storage mechanism in our HC follows an “adsorption-intercalation” process [58]. The corresponding sodium storage mechanism in HC is shown in Fig. 4(f). An analysis of the sodiation/desodiation capacity contribution at various cycles is shown in Fig. 4(g). The process of sodium insertion exhibits similarities was evidenced by some studies. It is characterized by two different regions: a slope region that extends to approximately 0.01 V and a low potential plateau region. The first step involves the insertion of alkaline ions between layers, where turbostratic disorder creates sites with various chemical environments, resulting in a sloping profile. The second step is associated with the adsorption of ions in micropores [50]. The slope capacity of HP-NHC was determined to be 363, 161, 164, 149, 174, and 176 mAh g^{-1} at the 1st, 5th, 10th, 50th, 100th and 200th cycles, respectively. The plateau capacity of HP-NHC was 219, 151, 140, 144, 151 and 158 mAh g^{-1} at the 1st, 5th, 10th, 50th, 100th and 200th cycles, respectively. The findings revealed that surface defect sites of charge gradient during the investigation were the main factor impeding Na^+ diffusion [66]. From the 1st cycle of charge/discharge curves, the slope region capacities of HC-Bare, HT-NHC and HP-NHC for 66.5, 65.1 and 62.3 % of the total capacities, respectively. It represented that HP-NHC had more plateau region capacity, which could be attributed to the larger proportion of closed micropores in HP-NHC [70–72]. Fig. 4(h) shows cycle life tests of HCMs at 0.5 A g^{-1}. Among these samples, HP-NHC exhibited the highest reversible capacity of ~362 mAh g^{-1} at the first cycle, which was higher than HC-Bare (152 mAh g^{-1}) and HT-NHC (260 mAh g^{-1}). After 200 cycles, the reversible capacities of HC-Bare, HT-NHC and HP-NHC were 185, 316 and 335 mAh g^{-1}, respectively. Fig. 5(a-c) and Table 4 show electrochemistry impedance spectroscopy (EIS) and the correspoing fitting data of HC-Bare, HT-NHC and HP-NHC after 2.5 cycles of sodiation state (0.01 V). R_1 is the electrolyte resistance. R_2 and R_3 are the resistance of the SEI layer and the charge transfer resistance of the composite. As shown in Table 4, R_1 of HC-Bare, HT-NHC and HP-NHC were 8.5, 1.3 and 5.2 Ω, respectively. R_2 of HC-Bare, HT-NHC and HP-NHC were 222.2, 308.9 and 73.6 Ω,

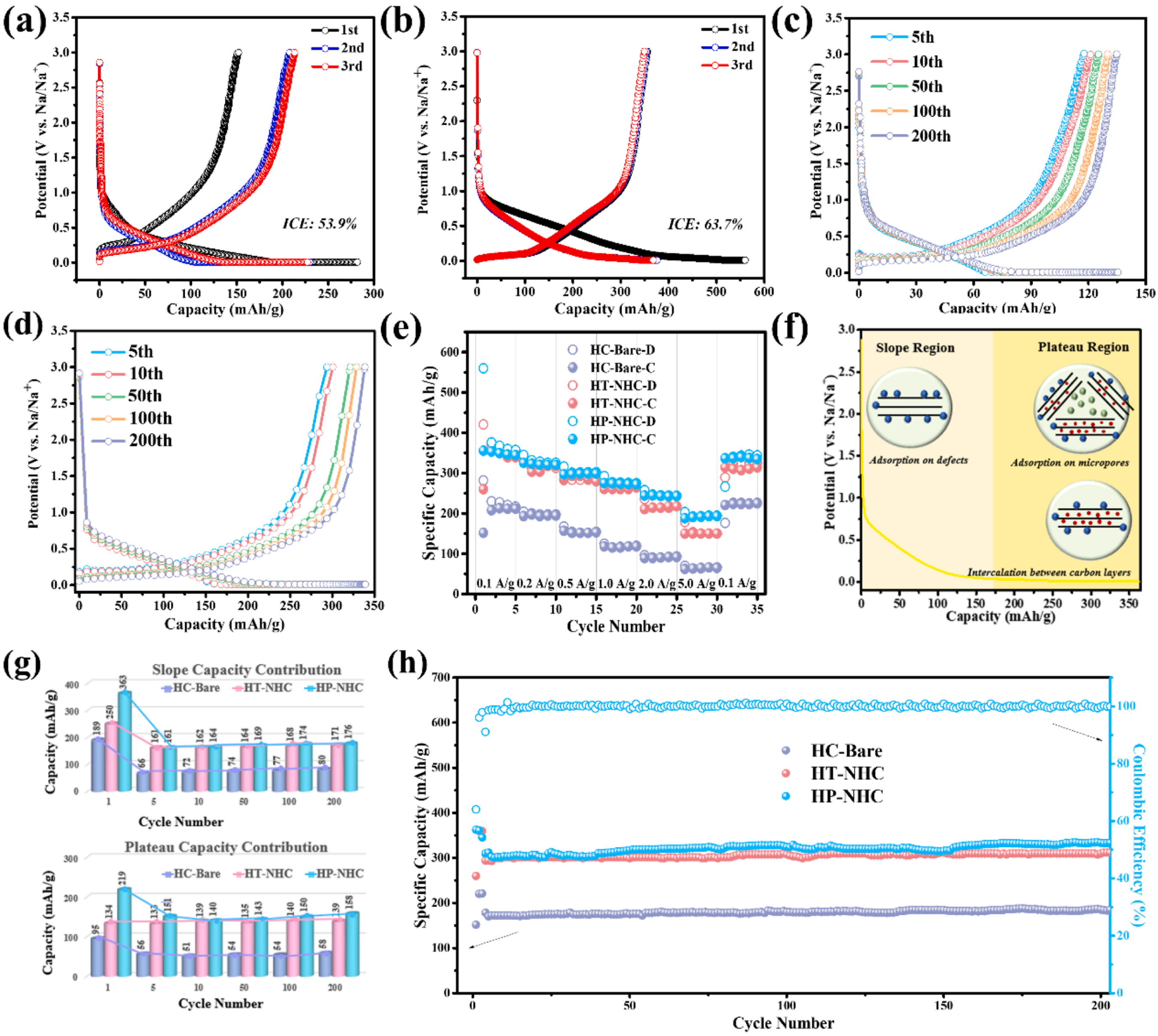

Fig. 4. (a) The initial galvanostatic charge/discharge curves of HC-Bare at 0.1 A/g; (b) The initial galvanostatic charge/discharge curves of HP-NHC; (c) Galvanostatic charge/discharge curves of HC-Bare at different cycles; (d) Galvanostatic charge/discharge curves of HP-NHC at the 5th, 10th, 50th, 100th and 200th cycles; (e) Rate performance of HCMs at 0.1, 0.2, 0.5, 1.0, 2.0, and 5.0 A g^{-1}; (f) Sodium-ion storage mechanism of HCMs; (g) Sodium-ion storage slope/plateau capacity contribution analysis; (h) Cycling performance of HCMs at 0.5 A g^{-1}.

respectively. There was a close correlation between the SSA and R_2, as an increase in SSA would increase to R_2. According to recent academic studies, less SSA may effectively minimize the formation of SEI (Solid Electrolyte Interphase) [49,57,59]. Due to the significant electrolyte breakdown that took place on the electrode surface during the first sodiation process, the irreversible capacity loss grew as the SSA of the electrode rose. R_3 of HC-Bare, HT-NHC and HP-NHC were 499.7, 106.3 and 134.0 Ω, respectively. Through the N-doping process, R_{ct} was significantly reduced, showing that N-doping could significantly improve the conductivity of carbon materials [41]. It could be explained from the XPS results that because the GN percentage of HT-NHC was higher than that of HP-NHC, the charge transfer resistance of HT-NHC was smaller. The charge transfer resistance mainly comes from the intercalation and deintercalation of Na^+. We speculated that after N doping processes, Na^+ can transfer more efficiently during the electrochemical processes due to the existence of N6, N5, NO and defects. To further identify Na^+ diffusivity in these three samples, we use the following equation to determine the diffusion coefficient (D) [50]:

$$D = \frac{R^2T^2}{2A^2n^4F^4C^2\sigma_W^2} \tag{2}$$

where R is the gas constant (J K^{-1} mol^{-1}), T is the temperature (K), n is the number of electrons per molecule during the oxidation process, A the electrode's surface area (cm^2), F is the Faraday constant (C mol^{-1}), C is the concentration of Na^+ (mol cm^{-3}), and σ_w is the Warburg factor, the relationship between the slope and the diffusion coefficient can be extracted. The diffusion coefficient increased with the decreasing slope of the connection between impedance and reciprocal root sign of frequency, as shown from the expression. The calculated D of HCMs is demonstrated in Fig. 5(d). The D of HC-Bare, HT-NHC and HP-NHC were 1.5×10^{-13}, 2.0×10^{-13}, and 5.2×10^{-13} cm^2/s, respectively. The D of HP-NHC was slightly higher than those of HC-Bare and HT-NHC. The results showed that HP-NHC exhibited desirable characteristics, such as

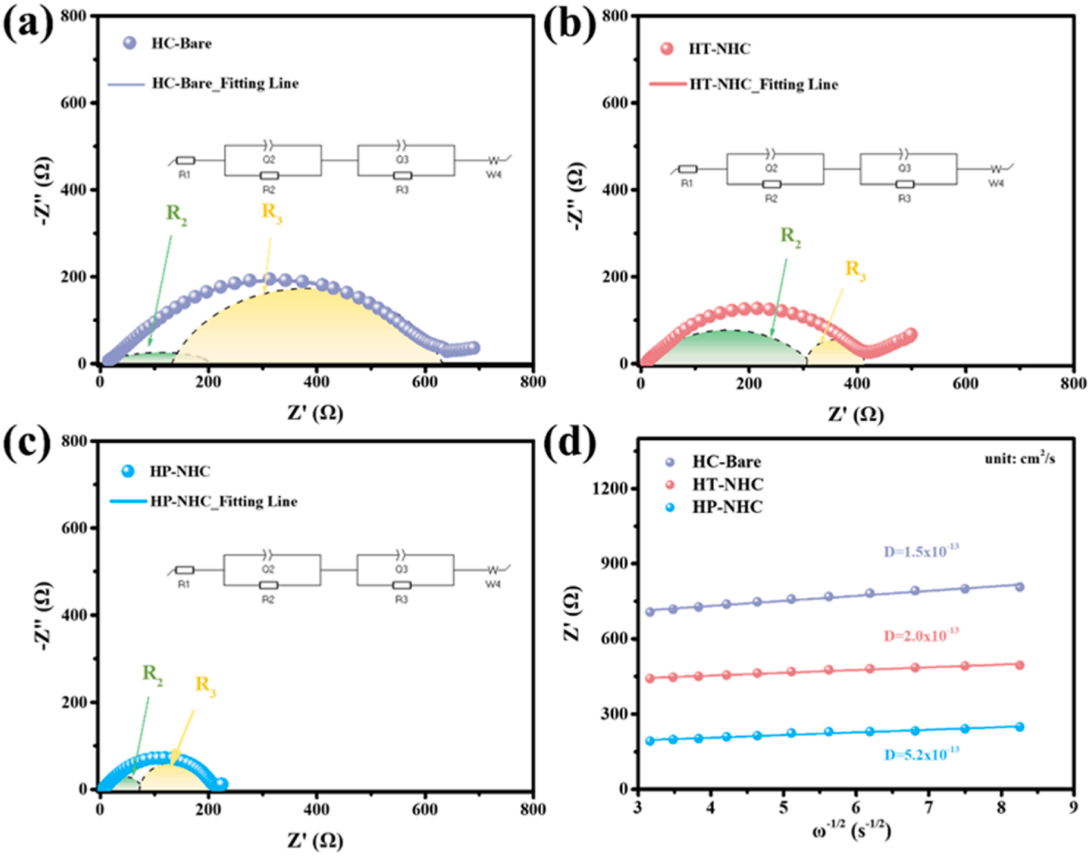

Fig. 5. (a) Electrochemical impedance spectra of HCMs at 2.5 cycles; Inset in (a): Equivalent circuit; (b) Z`-ω$^{-1/2}$ curves in the low-frequency region of each electrode after 2.5 cycles.

Table 4
Electrochemical impedance parameters of HCMs calculated from equivalent circuit model.

Samples	R_1 (Ω)	R_2 (Ω)	R_3 (Ω)
HC-Bare	1.2	222.2	499.7
HT-NHC	8.2	308.9	106.3
HP-NHC	5.2	73.6	134.0

larger D-interlayer spacing, degree of defect, and close pore structure, resulting in remarkable performance during charge and discharge processes [56].

Fig. 6(a) and (d) display cyclic voltammograms (CV) of HC-Bare and HP-NHC with 0.1 mV s^{-1} for the first three cycles and Fig. S6(c) shows CV curves of HT-NHC at the same condition. The SEI formation resulted from the decomposition of liquid electrolytes on the surface of the electrode, which occurred at around 0.4–0.6 V in the early reduction process. The plateau and slope portions of the measured CV curves were the razor-sharp peaks at 0.1 V and the moderately broad peak between 0.2–1.7 V. The CV curves of HCMs at the 2nd and 3rd cycles showed significant overlap, indicating that there were no apparent changes in the electrochemical reaction between the successive two cycles. The degree of polarization could be evaluated by determining the difference in the potential (ΔV) between the oxidation peak and reduction peak. Polarization occurs due to differences in electronic and ionic transportation rates and requires significant potential differences to compensate. The CV curves of HC-Bare and HP-NHC are shown in Fig. 6 (b) and (e) at various scan rates (0.1–0.5 mV s^{-1}) and the CV curves of HT-NHC are demonstrated in Fig. S6(d). As shown in Fig. 6(b) and (e) and Fig. S6(d), ΔV of HC-Bare, HT-NHC and HP-NHC were 0.3 V, 0.08 and 0.06 V, respectively, indicating that the polarization of HC-Bare was more severe than that of HT-NHC and HP-NHC [67–68]. The result was consistent with the EIS analysis shown in Fig. 5. In addition, Fig. 6(c) and (f) illustrate the D of HC-Bare and HP-NHC could also be obtained by Eq. (3) [56]:

$$I_p = 2.69 \times 10^5 n^{3/2} A D^{1/2} C v^{1/2} \tag{3}$$

where I_p is the peak current, n is the number of electrons transferred in a redox cycle, A is the electrode's surface area in the working electrode (cm^2), D is the diffusion coefficient (cm^2 s^{-1}), v is the scan rate (mV s^{-1}). The D_{Charge} and $D_{\mathrm{Discharge}}$ of HC-Bare were 9.15×10^{-10} and 9.73×10^{-10} cm^2/s, respectively. The D_{Charge} and $D_{\mathrm{Discharge}}$ of HP-NHC were 2.1×10^{-9} and 1.9×10^{-9} cm^2/s, respectively. Figure. S6(e) displays the D_{Charge} and $D_{\mathrm{Discharge}}$ of HT-NHC. The D_{Charge} and $D_{\mathrm{Discharge}}$ of HT-NHC were 1.5×10^{-9} and 1.6×10^{-9} cm^2/s, respectively. The D_{Charge} and $D_{\mathrm{Discharge}}$ of HT-NHC and HP-NHC were higher than that of HC-Bare. Similar D trends were observed in both the CV tests and the EIS analyses. Subsequently, we also calculated the diffusion-controlled and capacitive-controlled contribution of HP-NHC, which is displayed in Fig. 6(a-d). We calculated b by Eq. (4) [50],

$$i = av^b \tag{4}$$

Where i is the measured current, v is the scan rate and the values of a and b can be adjusted (as shown in Fig. 6(g)). When the b value is close to 0.5, the Na$^+$ storage mechanism is attributed to intercalation [25]. On the contrary, the Na$^+$ storage mechanism is attributed to the surface adsorption mechanism when the b value is close to 1.0. The b value from peak 1 at 0.3 V was calculated as 0.58. The b value from the peak 2 at 0.36 V was calculated as 0.67. The b value from the peak 3 at 0.01 V was calculated as 1.01. Furthermore, we also calculated the contribution by the Eq. (5) [56],

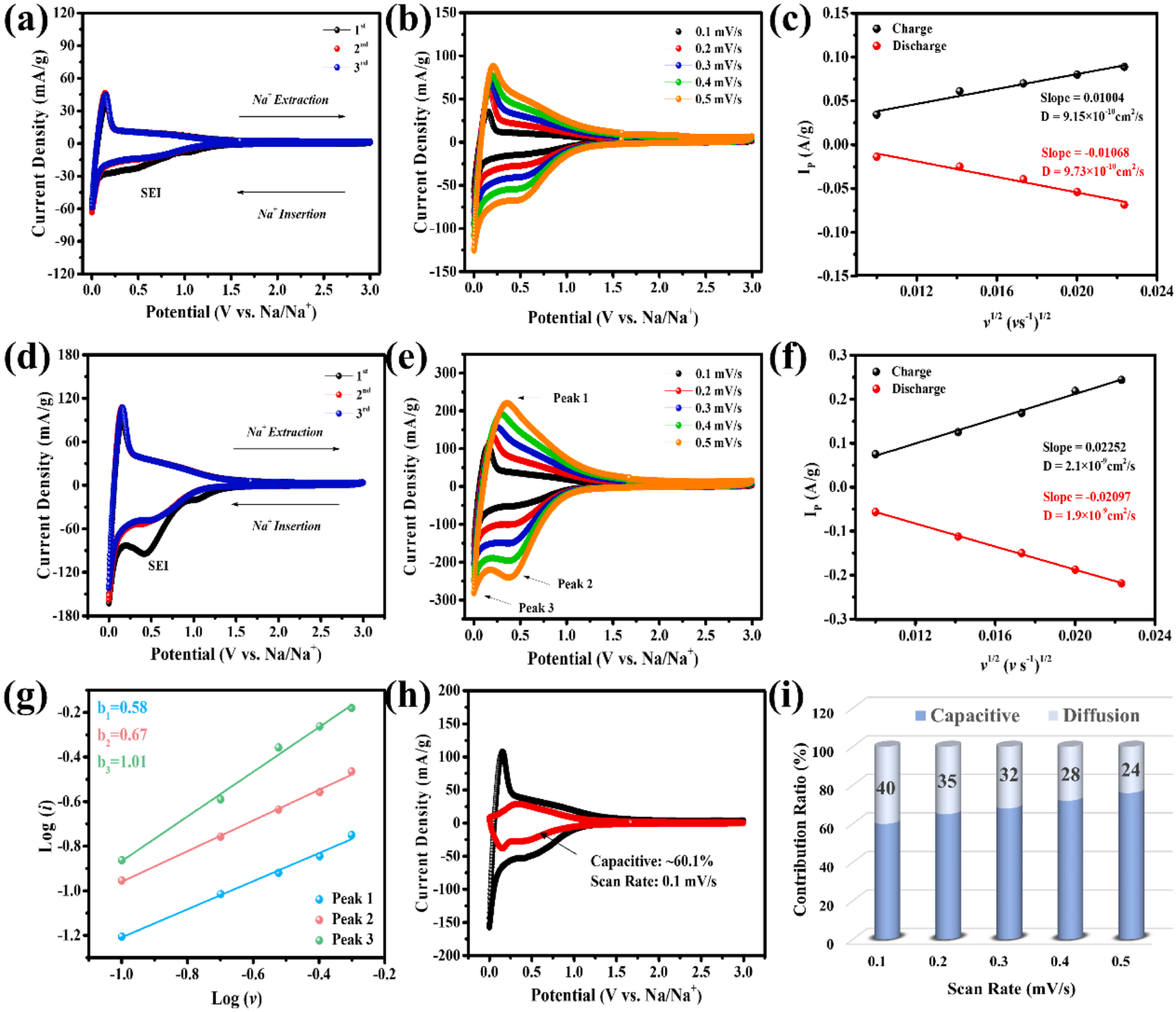

Fig. 6. CV curves of (a) HC-Bare and (c) HP-NHC at a scan rate of 0.1 mV s^{-1} for the first three cycles; (b) CV curves of HC-Bare at various scan rates from 0.1 mV s^{-1} to 0.5 mV s^{-1}; (e) CV curves of HP-NHC at various scan rates from 0.1 mV s^{-1} to 0.5 mV s^{-1}; (c) and (f) The linear relationship between the peak current and the square root of the scan rate at the reduction peak of HC-Bare and HP-NHC, respectively; (g) Fitting slope *b* value of HP-NHC from Fig 5. (e); (h) Calculating capacitive-controlled contributions of HP-NHC at 0.1 mV s^{-1}; (i) Diffusion-controlled capacity and contribution ratio of the capacitive versus scan rate.

$$I(v) = k_1 v + k_2 v^{1/2} \qquad (5)$$

k_1 and k_2 can be calculated by measuring various scan rates. where $k_1 v$ is surface limited capacitive effect and $k_2 v^{1/2}$ belongs to the diffusion control. The calculated capacitance contribution (red area) of the HP-NHC was 60, 65, 68, 72 and 76 % at scan rates of 0.1, 0.2, 0.3, 0.4 and 0.5 mV s^{-1}, respectively (as shown in Fig. 6(h-i)). We also calculated the capacitance contribution (red area) of the HT-NHC; it was displayed at 59, 66, 73, 75 and 80 %, respectively, at the same condition in Fig. S6 (g-h). The calculations revealed that the mechanism of Na^+ in HT-NHC and HP-NHC were both capacitive-controlled and diffusion-controlled, which was similar to the charge/discharge curve results shown in Fig. 4(a-b) [69].

We also investigated the effects of functional groups on Na-ion adsorption in HT-NHC and HP-NHC, utilizing first-principles calculations. The HT-NHC and HP-NHC contain N-functional groups from the doping process but than HC-Bare, as depicted in Table 2. The model systems were developed based on the assumption that a single layer of graphene can describe the impact of functional groups on the adsorption of Na^+ on HC, as illustrated in Fig. 7(a). Our findings indicated that the adsorption of Na^+ on graphene and graphitic N was thermodynamically unstable, as shown in Fig. 7(b). Among the functional groups, pyrrolic N exhibited the most favorable adsorption of the Na^+ compared to others, as demonstrated in Fig. 7(b). The pCOHP based on Density of States (DOS) for Na-adsorbed layers provided insight into the thermodynamic stability of the adsorbed Na^+. The pCOHP between Na^+ and graphitic N showed the anti-bonding states near the fermi level while, bonding states appear below -3 eV from the fermi level in pCOHP between Na^+ and pyridinic N (Fig. 7(c)). The graphene had the anti-bonding peak near the fermi level, leading to unfavorable adsorption of Na in Fig. S7. The other functional groups having negative adsorption energy exhibited bonding states below the Fermi level. The Lowdin charge corroborated the thermodynamic stability of Na on the surfaces. The 0.95e of Na^+ charge was distributed on GN and graphene surfaces, as represented in Fig. 7(d) and Fig. S8(a). The charge of Na^+, which was depleted in the range between 0.84e and 0.89e, had strong interactions with the

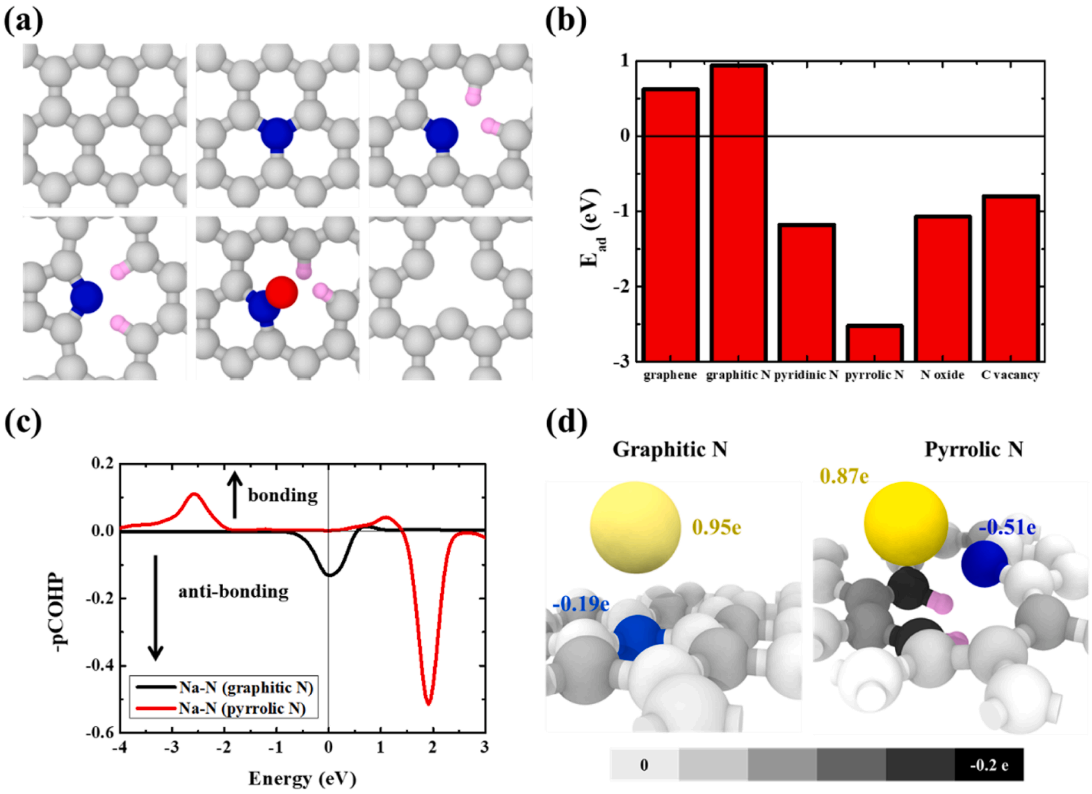

Fig. 7. (a) The model systems of graphene, Graphitic N and Pyridinic N (left to right on top) and Pyrrolic N, N-oxide and C vacancy (left to right on bottom) describing functional group effect of the hard carbon on Na adsorption; (b) Adsorption of Na^+ depending on the functional groups; (c) Projected crystal orbital Hamilton populations (pCOHP) and (d) Lowdin charges on Graphitic N and Pyrrolic N surfaces, respectively. The color bar in (d) represents the charge of the C atom. It should be noted that grey, blue, red, pink and yellow represent C, N, O, H and Na atoms, respectively.

functional groups of pyrrolic N (Fig. 7(d)), pyridinic N, N-oxide and C vacancy (Fig. S8). The over-oxidation of Na atom on graphene and graphitic N arose, occupying the anti-bonding state. Our study concluded that the pyrrolic N and other N-doped functional groups (pyridinic N, N-oxide and C vacancy) introduced favorable adsorption sites for Na^+, thereby enhancing the capacity of HT-NHC and HP-NHC, as supported by our experimental results.

Subsequently, we assembled a $Na_3V_2(PO_4)_3$/HP-NHC pouch-type full cells to evaluate the practical applications in industry. The charge/discharge curves at different current densities are shown in Fig. 8(a). At various current densities, HP-NHC performance was assessed in terms of rate performance (Fig. 8(b)), the discharge curves at various cycles (Fig. 8(c)), and cycle performance (Fig. 8(d)). Gradually, the current density was raised from 0.2 to 0.5, 1.0, 1.5 and 2.0C. The average reversible capacity of the pouch cell, as shown in Fig. 8(b), was 2.72, 2.52, 2.31, 2.20 and 2.10 mAh, respectively. It was discovered that the CE was over 99.0 % after 200 cycles.

HP-NHC involved N-doping through a hydrothermal high-pressure process, where nitrogen atoms were incorporated into the structure of HC at low temperatures with high pressures. Electrochemical tests confirmed our assumptions; the analysis of Fig. 4(f-g) revealed that in the charge and discharge tests at the first cycle, the reversible capacity of HC-Bare was only 284 mAh/g, with 66 % of the capacity contributed by the slope capacity and 34 % by the plateau capacity. Interestingly, the first-cycle capacity of HT-NHC increased to 384 mAh/g, with 65 % from slope capacity and 35 % from plateau capacity, showing a similar distribution. However, HP-NHC dramatically increased its reversible capacity to 582 mAh/g in the first cycle, with a significant 38 % contribution from the plateau capacity, i.e., the closed pores. After 200 cycles, the reversible capacities of HC-Bare and HT-NHC decreased to 138 mAh/g and 310 mAh/g, respectively, with their plateau capacity contributions increasing to 41 % and 44 %. This indicated that the open pore structures (Slope capacity contribution) of HC materials gradually deteriorated within the 200 cycles. Surprisingly, HP-NHC maintained a specific capacity of 336 mAh/g after 200 cycles, and, unexpectedly, its plateau capacity contribution was greater than that of HT-NHC, reaching 47 %. Such findings are believed to provide valuable insights for future inspirations in the structural design of HC anode materials.

To understand the sodium ion storage mechanisms of two different N-doped hard carbons, we proposed the possible sodium ion storage mechanisms of HP-NHC and HT-NHC, as shown in Fig. 9(a) and (b), respectively. HP-NHC involved N-doping through a hydrothermal high-pressure process, where N atoms were incorporated into the structure of HC at low temperatures with high pressures. Under high-pressure hydrothermal conditions, N atoms were squeezed and filled into the edge planes and surface open pores of HC material. BET results indicated a lower SSA attributed to the predominantly closed pore structure obtained through this high-pressure N doping process, as verified by Fig. 1 [59]. On the other hand, HT-NHC involved N-doping at a high temperature of 800 °C because the high-temperature process caused the structure collapse. Fig. 4(a-b) and Fig. 4(f-g) revealed that in the charge/discharge tests for the first cycle, the reversible specific capacity of HC-Bare was only 152 mAh/g, with 66 % of the capacity contributed by the slope-region capacity and 34 % by the plateau-region capacity. Interestingly, the first cycle capacity of HT-NHC increased to 260 mAh/g, with 65 % from slope-region capacity and 35 % from plateau-region capacity, showing a similar distribution. However, HP-NHC dramatically increased its reversible capacity to 362 mAh/g at the first cycle, with a significant 38 % contribution from the charge and discharge curves, i.e., the closed pores. After 200 cycles, the reversible capacities of HC-Bare and HT-NHC decreased to 138 mAh/g and 310 mAh/g, respectively, with their plateau-region capacity contributions increasing to 41 % and 44 %. This indicated that the open pore structures (Slope-region capacity contribution) of HC materials gradually

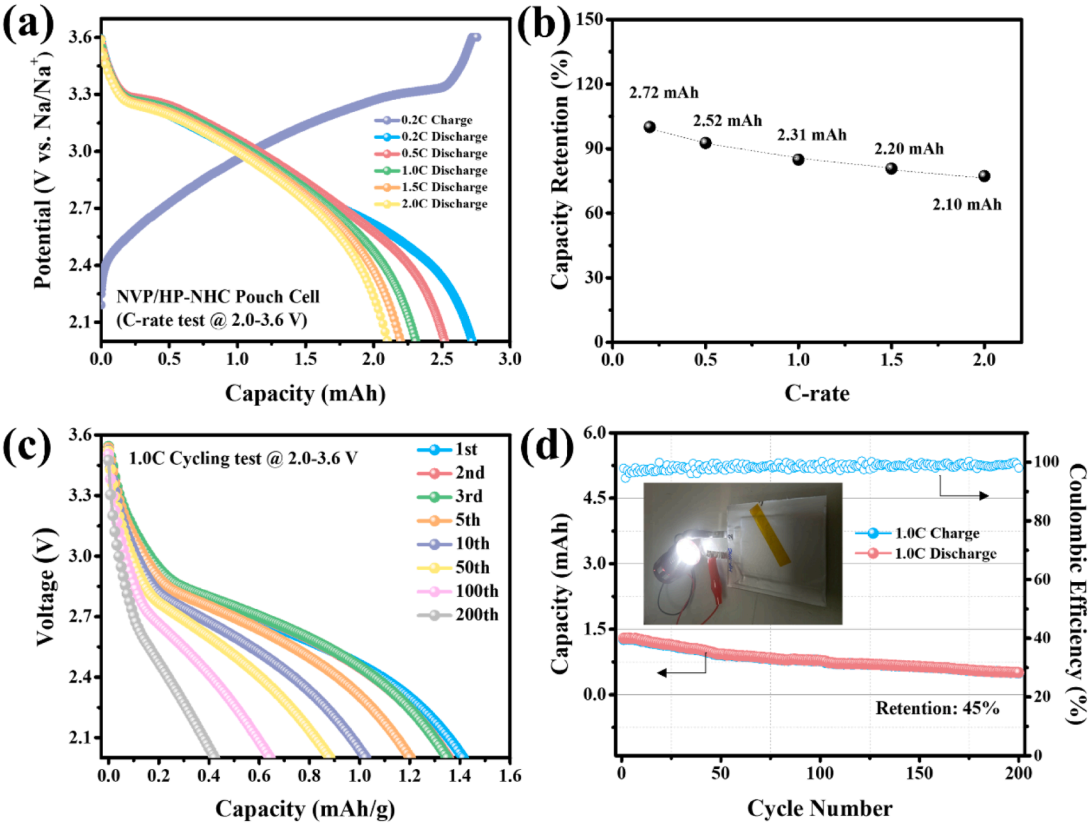

Fig. 8. (a) Galvanostatic charge/discharge curves of pouch cell at 0.2C charge, 0.2 C, 0.5C, 1.0C, 1.5C and 2.0C discharge; (b) Reversible capacity and the capacity retention of pouch cell at different current density; (c) Discharge curves of pouch cell for different cycles; (d) Cycle performance of pouch cell at 1.0C for 200 cycles (Inset: The image of pouch cell).

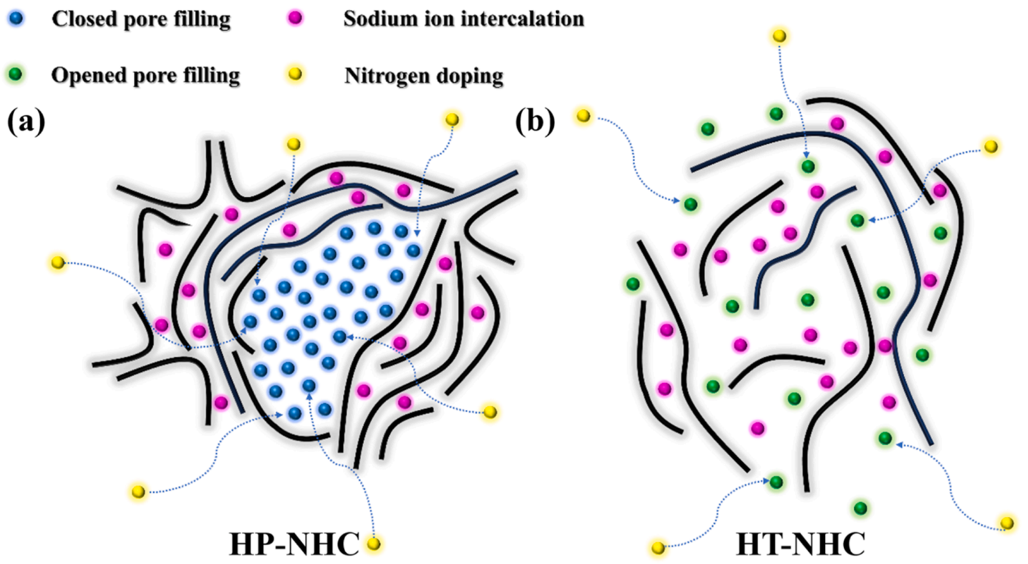

Fig. 9. Schematic illustrations of the Na$^+$ storage mechanism in (a) HP-NHC and (b) HT-NHC.

deteriorated after 200 cycles. Surprisingly, HP-NHC maintained a capacity of 336 mAh/g after 200 cycles, and its plateau-region capacity contribution was unexpectedly greater than that of HT-NHC, reaching 47 %. This suggested that closed pores play a crucial role in the stability of HC-anode materials during long cycling lifetimes. Such findings are believed to provide valuable insights for future inspirations in the structural design of HC anode materials.

4. Conclusions

In this study, HC-Bare was used to conduct experiments and modified via two nitrogen doping techniques as an anode material for SIBs. Closed pores can greatly lower the initial irreversible capacity and facilitate the intercalation of Na$^+$ by limiting solvent penetration. The results indicated that the electrochemical performance was improved with a higher pyridinic N content. Pyridinic N can behave as the active site for electrochemical processes. N6 can enhance the performance of electrodes in energy storage devices like SIBs by facilitating charge transfer and boosting electrochemical activity. The electrochemical investigation showed that both diffusion-controlled and capacitive-controlled processes are critical for Na^+ transfer. As a result, the Na^+, G and GN surfaces contact weakly electrostatically. Our theoretical calculations corroborate our findings, which show that the N5 and other N-doped functional groups (N6, NO, and D) create suitable adsorption sites for Na^+, increasing the capacity of HT-NHC and HP-NHC. Among these samples, HP-NHC exhibited the best reversible capacity of 351 mAh/g at 0.1 A/g, excellent rate capability of 193 mAh/g at 5.0 A/g, and stable cycle performance of CE~99.99 % after 200 cycles, confirming the effect of N-doping on the sodium storage mechanism in SIBs. Finally, we also used HP-NHC as anode material and NVP as cathode material to prepare pouch cells. The results indicated that HP-NHC was an excellent candidate for anode materials in SIBs.

CRediT authorship contribution statement

Zhi-Ting Liu: Writing – original draft, Formal analysis, Data curation. **Tzu-Hsien Hsieh:** Formal analysis. **Cheng-Wei Huang:** Formal analysis. **Choah Kwon:** Formal analysis. **Ju Li:** Writing – review & editing. **Jun-Yang You:** Formal analysis. **Chin-Jung Lin:** Formal analysis. **Wei-Ren Liu:** Writing – review & editing, Supervision, Conceptualization.

Declaration of competing interest

The authors declare that they have no known competing financial interests or personal relationships that could have appeared to influence the work reported in this paper.

Acknowledgments

The authors gratefully acknowledged to National Science of Technology Council (NSTC) project grant no NSTC 111–2622-E-033–007, 111–2811-E-033–001-MY3, 111–2221-E-033 –004 -MY3, 111–2923-E-006–009, 111–3116-F-011–005, NSTC 111–2222-E-131–002, 112–2218-E-007–023, 112–2923-E-006–004 and 112–2622-E-033–013. This work was financially supported by the Hierarchical Green-Energy Materials (Hi-GEM) Research Center, from The Featured Areas Research Center Program within the framework of the Higher Education Sprout Project by the Ministry of Education (MOE) in Taiwan.

Supplementary materials

Supplementary material associated with this article can be found, in the online version, at doi:10.1016/j.electacta.2025.146552.

Data availability

No data was used for the research described in the article.

References

[1] M.V. Reddy, A. Mauger, C.M. Julien, A. Paolella, K. Zaghib, Mater. 13 (2020) 1884–1893.
[2] L.Nicoletti König, D. Schröder, S. Wolff, A. Waclaw, M. Lienkamp, World Electr. Veh. J. 12 (2021) 21–50.
[3] A. Eftekhari, ACS Sustain. Chem. Eng. 7 (2019) 5602–5613.
[4] X.B. Cheng, H. Liu, H. Yuan, H.J. Peng, C. Tang, J.Q. Huang, Q. Zhang, SusMat. 1 (2021) 38–50.
[5] M. Armand, P. Axmann, D. Bresser, M. Copley, K. Edström, C. Ekberg, D. Guyomard, B. Lestriez, P. Novák, M. Petranikova, W. Porcher, S. Trabesinger, M. W. Mehrens, H. Zhang, J. Power Sources 479 (2020) 228708.
[6] A. Mayyas, D. Steward, M. Mann, Sustain. Mater.Technol. 19 (2019) e00087.
[7] E. Fan, L. Li, Z. Wang, J. Lin, Y. Huang, Y. Yao, R. Chen, F. Wu, Chem. Rev. 120 (2020) 7020–7063.
[8] A.R. Dehghani-Sanij, E. Tharumalingam, M.B. Dusseault, R. Fraser, Renew. Sust. Energ. Rev. 104 (2019) 192–208.
[9] Y. Fang, L. Xiao, Z. Chen, X. Ai, Y. Cao, H. Yang, Electro. Ener. Rev. 1 (2018) 294–323.
[10] M. Chen, Q. Liu, S.W. Wang, E. Wang, X. Guo, S.L. Chou, Adv. Energy Mater. 9 (2019) 1803609.
[11] Y. Fang, X.Y. Yu, X.W.D. Lou, Matter 1 (2019) 90–114.
[12] X. Zheng, C. Bommier, W. Luo, L. Jiang, Y. Hao, Y. Huang, Energy Stor. Mater. 16 (2019) 6–23.
[13] T. Liu, Y. Zhang, Z. Jiang, X. Zeng, J. Ji, Z. Li, X. Gao, M. Sun, Z. Lin, M. Ling, J. Zheng, C. Liang, Energy Environ. Sci. 12 (2019) 1512–1533.
[14] Z. Chen, D. Zhu, J. Li, D. Liang, M. Liu, Z. Hu, X. Li, Z. Feng, J. Huang, Ionics 25 (2019) 4517–4522.
[15] R. Usiskin, Y. Lu, J. Popovic, M. Law, P. Balaya, Y.S. Hu, J. Maier, Nat. Rev. Mater. 6 (2021) 1020–1035.
[16] C. Vaalma, D. Buchholz, M. Weil, S. Passerini, Nat. Rev. Mater. 3 (2018) 1–11.
[17] P. Li, N. Hu, J. Wang, S. Wang, W. Deng, Nanomaterials 12 (2022) 3529.
[18] D. Alvira, D. Antorán, J.J. Manyà, Chem. Eng. J. (2022) 137468.
[19] X. Dou, I. Hasa, D. Saurel, C. Vaalma, L. Wu, D. Buchholz, S. Komaba, S. Passerini, Mater. Today 23 (2019) 87–104.
[20] M. Zhang, Y. Li, F. Wu, Y. Bai, C. Wu, Nano Energy 82 (2021) 105738.
[21] S. Sekar, Y. Lee, D.Y. Kim, S. Lee, Nanomaterials 9 (2019) 871.
[22] Y. Quan, D. Han, Y. Feng, S. Wang, M. Xiao, Y. Meng, Int. J. Electrochem. Sci. 12 (2017) 5984–5997.
[23] V. Mullaivananathan, R. Sathish, N. Kalaiselvi, Electrochim. Acta 225 (2017) 143–150.
[24] R. Muruganantham, F.M. Wang, R.A. Yuwono, M. Sabugaa, W.R. Liu, Energy Fuels 35 (2021) 10878–10889.
[25] V. Selvamani, R. Ravikumar, V. Suryanarayanan, D. Velayutham, S. Gopukumar, Electrochim. Acta 190 (2016) 337–345.
[26] J. Xiang, W. Lv, C. Mu, J. Zhao, B. Wang, J. Alloys Compd. 701 (2017) 870–874.
[27] D. Damodar, S. Ghosh, M.U. Rani, S.K. Martha, A.S. Deshpande, J. Power Sources 438 (2019) 227008.
[28] N. Zhang, Q. Liu, W. Chen, M. Wan, X. Li, L. Wang, L. Xue, W. Zhang, J. Power Sources 378 (2018) 331–337.
[29] I. Elizabeth, B.P. Singh, S. Trikha, S. Gopukumar, J. Power Sources 329 (2016) 412–421.
[30] M. Dahbi, M. Kiso, K. Kubota, T. Horiba, T. Chafik, K. Hida, T. Matsuyama, S. Komaba, J. Mater. Chem. A 5 (2017) 9917–9928.
[31] T. Lyu, L. Liang, P.K. Shen, J. Colloid Interface Sci. 604 (2021) 168–177.
[32] L. Qu, Y. Liu, J.-B. Baek, L. Dai, ACS Nano 4 (2010) 1321–1326.
[33] D. Wei, Y. Liu, Y. Wang, H. Zhang, L. Huang, G. Yu, Nano Lett. 9 (2009) 1752–1758.
[34] Y. Wang, Y. Shao, D.W. Matson, J. Li, Y. Lin, ACS Nano 4 (2010) 1790–1798.
[35] B. Guo, Q. Liu, E. Chen, H. Zhu, L. Fang, J.R. Gong, Nano Lett. 10 (2010) 4975–4980.
[36] Q. Jin, K. Wang, P. Feng, Z. Zhang, S. Cheng, K. Jiang, Energy Stor. Mater. 27 (2020) 43–50.
[37] L. Qie, W. Chen, X. Xiong, C. Hu, F. Zou, P. Hu, Y. Huang, Adv. Sci. 2 (2015) 1500195.
[38] Q. Jin, W. Li, K. Wang, P. Feng, H. Li, T. Gu, M. Zhou, W. Wang, S. Cheng, K. Jiang, J. Mater. Chem. A 7 (2019) 10239–10245.
[39] D. Li, D. Wang, K. Rui, Z. Ma, L. Xie, J. Liu, W. Huang, J. Power Sources 384 (2018) 27–33.
[40] H.Y. Lu, X.H. Zhang, F. Wan, D.S. Liu, C.Y. Fan, H.M. Xu, G. Wang, X.L. Wu, ACS Appl. Mater. Interfaces 9 (2017) 12518–12527.
[41] P.M. Ting, J.Y. Huang, R. Muruganantham, W.R. Liu, Mater. Today Commun. 31 (2022) 103498.
[42] P. Han, Y. Yue, L. Zhang, H. Xu, Z. Liu, K. Zhang, C. Zhang, S. Dong, W. Ma, G. Cui, Carbon N Y 50 (2012) 1355–1362.
[43] H. Lim, H. Kim, S.O. Kim, W. Choi, Chem. Eng. J. 387 (2020) 124144.
[44] W. Chen, M. Wan, Q. Liu, X. Xiong, F. Yu, Y. Huang, Small Methods 3 (2019) 1800323.
[45] F. Bergius, Zeitschrift fur Komprimierte und Flussige Gase, 1915, 17.
[46] M.M. Titirici, R.J. White, N. Brun, V.L. Budarin, D.S. Su, F. Del Monte, J.H. Clark, M.J. MacLachlan, Chem. Soc. Rev. 44 (2015) 250–290.
[47] L. Zhao, N. Baccile, S. Gross, Y.J. Zhang, W. Wei, Y.H. Sun, M. Antonietti, M. M. Titirici, Carbon N Y 48 (2010) 3778–3787.
[48] Y.V. Fedoseeva, E.V. Lobiak, E.V. Shlyakhova, K.A. Kovalenko, V.R. Kuznetsova, A. A. Vorfolomeeva, M.A. Grebenkina, A.D. Nishchakova, A.A. Makarova, L. G. Bulusheva, A.V. Okotrub, Nanomaterials 10 (2020) 2163.
[49] W. Nie, H. Cheng, X. Liu, Q. Sun, F. Tian, W. Yao, S. Liang, X. Lu, J. Zhou, J. Power Sources 522 (2022) 230994.
[50] Z.T. Liu, T.H. Hsieh, C.W. Huang, M.L. Lee, W.R. Liu, J. Taiwan Inst. Chem. Engrs. (2023) 104889.
[51] G. Kresse, J. Hafner, Phys. Rev. B 47 (1994) 558, ibid.49, 14251.
[52] G. Kresse, J. Furthmüller, Comput. Mat. Sci. 6 (1996) 15.
[53] I.G. Kresse, D. Joubert, Phys. Rev. B 59 (1999) 1758.
[54] J.P. Perdew, K. Burke, M. Ernzerhof, Phys. Rev. Lett. 77 (1996) 3865.
[55] S. Grimme, J. Antony, S. Ehrlich, S. Krieg, J. Chem. Phys. 132 (2010) 154104.
[56] J. Li, J. Song, L. Luo, H. Zhang, J. Feng, X. Zhao, Guo X, H. Dong, S. Chen, H. Liu, G. Shao, T.D. Anthopoulos, Y. Su, G. Wang, Adv. Energy Mater. 12 (2022) 2200894.
[57] N. Sun, Z. Guan, Y. Liu, Y. Cao, Q. Zhu, H. Liu, Z. Wang, P. Zhang, B. Xu, Adv. Energy Mater. 9 (2019) 1901351.

[58] R. Hou, B. Liu, Y. Sun, L. Liu, J. Meng, M.D. Levi, H. Ji, X. Yan, Nano Energy 72 (2020) 104728.

[59] Z. Zhou, Z. Gu, Y. He, D. Peng, C. Bao, H. Liu, Int. J. Electrochem. Sci. 14 (2019) 6976–6985.

[60] L. Guo, M. Huang, W. Liu, H. Zhu, Y. Cheng, M.S. Wang, J. Mater. Chem. A 12 (2024) 13703.

[61] C.W. Tai, W.Y. Jao, L.C. Tseng, P.C. Wang, A.P. Tu, C.C. Hu, J. Mater. Chem. A 11 (2023) 19669–19684.

[62] Y. Lu, K.H. Shin, Y. Yu, Y. Hu, J. Liang, K. Chen, H. Yuan, H.S. Park, D. Wang, Adv. Funct. Mater. 31 (2021) 2007247.

[63] J. Ye, H. Zhao, W. Song, N. Wang, M. Kang, Z. Li, J. Power Sources 412 (2019) 606–614.

[64] X. Tian, Z. Jiang, X. Shuang, X. Gu, T. Maiyalagan, Z.J. Jiang, Int. J. Hydrog. Energy 45 (2020) 16569–16582.

[65] F. Sun, H. Wang, Z. Qu, K. Wang, L. Wang, J. Gao, S. Liu, Y. Lu, Adv. Energy Mater. 11 (2021) 2002981.

[66] B. Zhang, C.M. Ghimbeu, C. Laberty, C. Vix-Guterl, J.M. Tarascon, Adv. Energy Mater 6 (2016) 1501588.

[67] Y. Li, Y.S. Hu, M.M. Titirici, L. Chen, X. Huang, Adv. Energy Mater 6 (2016) 1600659.

[68] F. Yang, Y. Qiao, B. Gao, P. Duan, Y. Zhu, Ionics 22 (2016) 1603–1610.

[69] M. Nakayama, K. Iizuka, H. Shiiba, S. Baba, M. Nogami, J. Ceram. Soc. Japan 119 (2011) 692–696.

[70] Z. Zheng, S. Hu, W. Yin, J. Peng, R. Wang, J. Jin, B. He, Y. Gong, H. Wang, H.J. Fan, Adv. Energy Mater. 14 (2024) 2303064.

[71] X. Yin, Z. Lu, J. Wang, X. Feng, S. Roy, X. Liu, Y. Yang, Y. Zhao, J. Zhang, *Adv. Mater.* 34 (2022) 2109282.

[72] Z. Tang, R. Zhang, H. Wang, S. Zhou, Z. Pan, Y. Huang, D. Sun, Y. Tang, X. Ji, K. Amine, M. Shao, Nat. Commun. 14 (2023) 6024.

[73] Z. Zheng, S. Hu, W. Yin, J. Peng, R. Wang, J. Jin, B. He, Y. Gong, H. Wang, H.J. Fan, Adv. Energy Mater. 14 (2024) 2303064.

[74] D. Sun, L. Zhao, P. Sun, K. Zhao, Y. Sun, Q. Zhang, Z. Li, Z. Ma, F. Zheng, Y. Yang, C. Lu, C. Peng, C. Xu, Z. Xiao, X. Ma, Adv. Funct. Mater. 34 (2024) 2403642.

[75] Z. Tang, R. Liu, D. Jiang, S. Cai, H. Li, D. Sun, Y. Tang, H. Wang, ACS Appl. Mater. Interfaces 16 (2024) 47504–47512.

[76] D. Sun, L. Zhao, P. Sun, K. Zhao, Y. Sun, Q. Zhang, Z. Li, Z. Ma, F. Zheng, Y. Yang, C. Lu, C. Peng, C. Xu, Z. Xiao, X. Ma, Adv. Funct. Mater. 34 (2024) 2403642.

[77] Z. Tang, R. Liu, D. Jiang, S. Cai, H. Li, D. Sun, Y. Tang, H. Wang, ACS Appl. Mater. Interfaces 16 (2024) 47504–47512.